Event Localization in Bulk Scintillator Crystals Using Coded Apertures

K.P. Ziock[a,b,*], J.B. Braverman[b], L. Fabris[a], M.J. Harrison[a], D. Hornback[a], J. Newby[a]

[a]Oak Ridge National Laboratory, Oak Ridge, TN USA

[b]Department of Physics and Astronomy, University of Tennessee, Knoxville, TN, USA

Keywords: Scintillation Detector, Position-Sensitive Detector, Coded Aperture Imaging, Gamma-ray Detector

ABSTRACT

The localization of radiation interactions in bulk scintillators is generally limited by the size of the light distribution at the readout surface of the crystal/light-pipe system. By finding the centroid of the light spot, which is typically of order centimeters across, practical single-event localization is limited to ~2 mm/cm of crystal thickness. Similar resolution can also be achieved for the depth of interaction by measuring the size of the light spot. Through the use of near-field coded-aperture techniques applied to the scintillation light, light transport simulations show that for 3-cm-thick crystals, more than a five-fold improvement (millimeter spatial resolution) can be achieved both laterally and in event depth. At the core of the technique is the requirement to resolve the shadow from an optical mask placed in the scintillation light path between the crystal and the readout. In this paper, experimental results are presented that demonstrate the overall concept using a 1D shadow mask, a thin-scintillator crystal and a light pipe of varying thickness to emulate a 2.2-cm-thick crystal. Spatial resolutions of ~ 1 mm in both depth and transverse to the readout face are obtained over most of the crystal depth.

1. INTRODUCTION

Gamma-ray detectors based on inorganic scintillator crystals are widely used throughout the radiation detection community. Their useful balance of energy resolution, stopping power, and cost per unit volume has made them essential to a broad range of fields such as fundamental physics, high-energy astrophysics, homeland security, and nuclear medicine. In many of these applications, one is interested in both the energy of the gamma radiation and its interaction location within the detector. Several approaches have been developed to measure the latter. The most straightforward approach is to place a series of readout devices on one or multiple surfaces of a bulk crystal and look at how the light is shared between them. The location of each interaction is estimated using some form of centroiding algorithm with the spatial resolution limited by the size of the light spot at the readout surface divided by the square root of the number of detected scintillation photons. Anger cameras [1] are the primary example of this approach, and they can achieve a spatial resolution of a few millimeters along the instrumented face [2]. The problem with the centroiding approach is that the size of the light spot is of order the distance that the event occurs from the readout surface, and so the ability to locate the event is limited (~2 mm/cm of crystal thickness at 500 keV).

One means to improve spatial resolution is to subdivide the crystal to restrict the spread of the light to a single small “crystalet.” Using this approach, one can achieve better spatial resolution (<1 mm). However, if the crystalets are too small, then they will “leak” energy to neighboring locations due to finite electron ranges, K-escape peaks, and Compton scatter. Further, to provide good stopping power and maintain good spatial resolution requires crystalets with a high aspect ratio. This tends to limit energy resolution since fewer of the scintillation photons created in events far from the readout surface are detected.

When one requires the location of an event in all three dimensions, the problem becomes even harder. In detectors that use bulk crystals, one can determine the depth of an event by measuring the size of the light spot at the readout. This provides a resolution similar to that of an event’s lateral location. In segmented systems with high aspect crystalets, one can instrument both ends of the crystalet and use light sharing (or even light arrival time for larger bar pixels). The thickness of such an assembly will be limited by the acceptable light loss from multiple reflections along the crystalet. In small systems (~1 cm^3), sub-millimeter spatial resolution can be achieved, but with a significant increase in the system complexity [3].

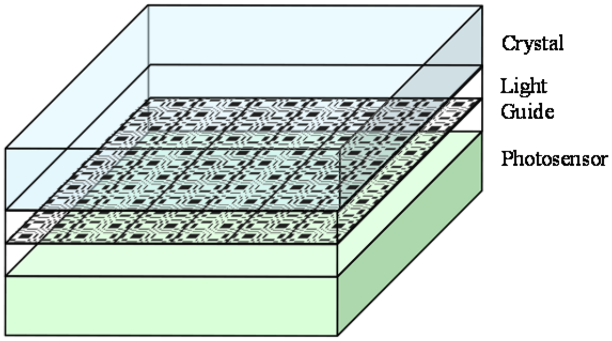

Fig. 1. Detector concept. An optical coded-aperture shadow mask is positioned in the light pipe connecting a bulk scintillator crystal with a position-sensitive photosensor.

We report the first experimental results of a new approach that promises to provide the spatial resolution achievable with a pixelated system in a bulk scintillator. The technique is shown schematically in Fig. 1. It uses a coded-aperture shadow mask [4] in the light pipe that connects the scintillator crystal to a position-sensitive readout device. The shadow mask encodes the event location in all three dimensions, allowing one to locate events within the crystal. For the location parallel to the readout surface, standard coded-aperture cross-correlation calculations are used [4]. To determine the depth of an event, the approach takes advantage of the fact that the mask pattern projected on the readout device is magnified, with the amount of magnification determined by the depth of the event within the crystal. By sequentially reconstructing an event at different depths (magnifications), one can *a posteriori* “vary the focus” of the system and look for the sharpest image. Extensive light-transport simulations have been conducted and indicate that voxel sizes of order a cubic millimeter can be achieved at energies as low as several hundred keV in 3-cm-thick scintillators [5,6]. For the first measurements reported here, a 1D coded aperture was used to provide 2D event reconstructions—depth and one dimension lateral to the readout surface.

2. EXPERIMENTAL DESIGN

A photograph and schematic of the hardware used for the experiment are shown in Fig. 2. In the experiment a thin scintillator crystal [1-mm-thick NaI(Tl), index of refraction n = 1.85] is mounted to a quartz light pipe (n = 1.458) that contains the shadow mask. Additional light pipe below the mask connects to the readout. Changing the amount of light pipe between the crystal and the mask provides a means of emulating a thick crystal with events located at different known depths.

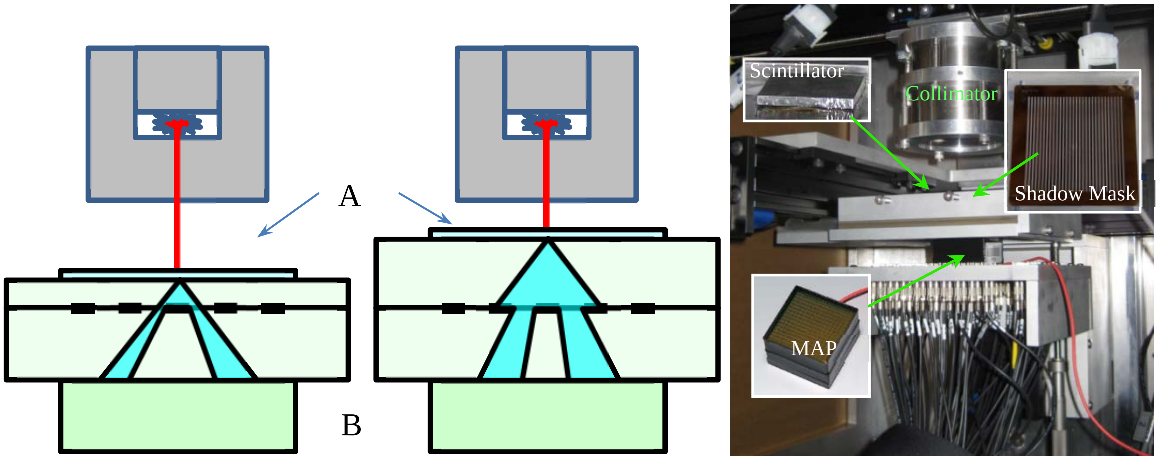

Fig. 2. Schematics of the experimental layout (left, center). A thin crystal (A) is placed on top of the light pipe/mask assembly. Scintillation light is detected by the MAP (B). The amount of light pipe between the mask and the crystal can be varied to emulate events at different locations within a thick crystal. Events at the bottom (left) generate a mask shadow with a greater magnification at the MAP compared to an event at the top of the crystal. The experimental hardware is shown on the right.

The experiment used three Hamamatsu 9500 multi-anode photomultiplier (MAP) tubes [7] arranged side by side. All of the anodes perpendicular to the three-tube axis were connected to form readout strips. This MAP array was used below a shadow mask based on multiple repetitions of a rank-7, 1D modified uniformly redundant array (MURA) coded aperture [8]. To localize the radiation to a given region of the crystal, a tungsten collimator was used. This provided a beam ~1.2 mm in diameter at the crystal surface. Connections between optical elements were made using optical coupling compound (n = 1.465) [9].

2.1 CRYSTAL THICKNESS

The maximum displacement of the thin crystal in the experiments was 14.7 mm. Because the angular divergence of the light cloud increases when transitioning into the quartz (index of refraction ~1.5) from the higher index scintillator (~1.8), a smaller thickness of quartz generates the same spread as a greater thickness of scintillator crystal. To obtain the conversion factor between event depths in a bulk scintillator and the thin-crystal-quartz-light-pipe analog, we ran light transport simulations using GEANT4 [10] similar to those reported earlier [5, 6]. In the simulations, a scintillation event was modelled by launching 40,000 photons at the top of the apparatus shown in Fig. 2. The photons were launched randomly in all directions. (Note that the top and sides of the optical system are painted black, and any photons hitting those surfaces were removed from the transport simulations.) The locations where photons reached the photocathode of the MAPs were recorded and mapped to the anode structure used in the experiment. These events were then imaged as described in Section 3.1.3 below to determine the event depth. For systems with different optical thicknesses, two configurations were run, one with a thin NaI(Tl) crystal with a quartz light pipe, and one where the light pipe was replaced by a material with the same refractive index as that of NaI. The results are plotted in Fig. 3 and show a linear relationship with a slope of 0.63. This factor is used in Table 1 to relate the real geometry to the emulated event location within a thick crystal. It indicates that the 15-mm-thick light pipe is comparable to a 22.5-mm-thick crystal.

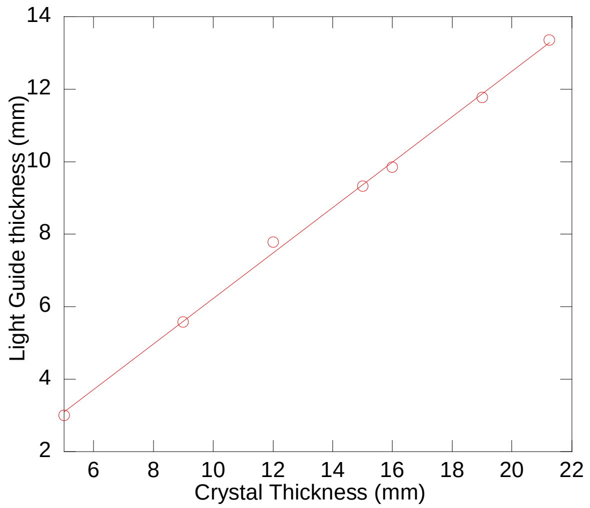

Fig. 3. Relationship between the thickness of the light pipe emulation and a bulk crystal.

2.2 READOUT SYSTEM

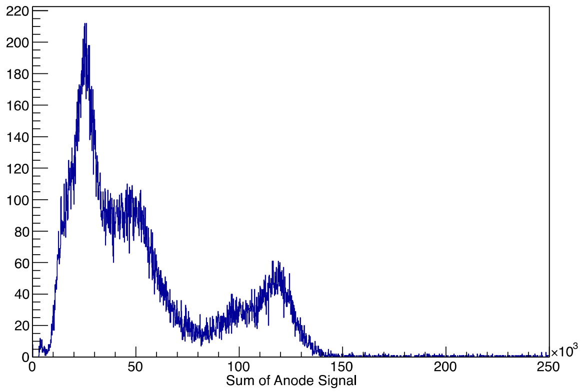

Fig. 4 Spectrum obtained from a ^{133}Ba source using the peaklet integration approach .

The design of the experiment was dominated by the 64 channels of readout available to perform the work. The data acquisition system comprised four, 250 MHz digitizers [11] in a VME crate read out using a personal computer. Due to noise and signal reflection issues when the digitizers were configured to run in a high-input impedance mode, the 50 Ω mode was used. To drive this the output of each row of anodes was sent through a Phillips 776, times 10 amplifier [12] before being passed to the digitizers. Residual baseline noise around 1 MHz meant that simply integrating the total charge received during the decay period of the scintillator light (a 3200-ns integration window was used) yielded poor energy resolution. To overcome this a modified peaklet analysis procedure was implemented. After a trigger was received (based on the signal from the last dynode of the center MAP), the 3200-ns-wide inspection window was opened for each channel. The signal recorded during the window was searched for the many small (single or a few) photoelectron pulses (peaklets) that arrived in each channel. The signal was integrated for those times that the signal level was above an empirically determined threshold that was set to avoid triggering on noise. With the threshold set high enough to avoid noise, some charge was lost in the bins immediately before and just after the signal rose above or fell below the threshold level. The integration routine was modified to explicitly include data from those time bins. This technique provided good energy resolution and was developed during initial tests with a single MAP to show that single photoelectrons could be detected. A sample energy spectrum of ^{133}Ba obtained by the system without a shadow mask in the light pipe is shown in Fig. 4. As expected, addition of the mask reduced the peak location due to the light blocked by the mask by a factor of two and worsened the energy resolution for the 356-keV peak from 14% full width at half maximum (FWHM) to 20% (~ root-two worse). These are reasonable values given that the crystal sides are polished and the top and sides of the crystal are painted black to reduce unwanted reflections from those surfaces that would make analysis of the shadow data more difficult.

2.3 MASK DESIGN

Optical masks with 2 μm of chromium on 6.35-mm-thick quartz blanks were purchased from a vendor [13] that supplies photomasks to the semiconductor industry. Specifications from the manufacturer indicate residual transmission at 410 nm of only 0.032%. One side of the masks is shiny, and this surface was oriented away from the crystal. A rank-7 MURA coded aperture [8] was chosen with a pixel pitch of 1.4 mm (Fig. 5).

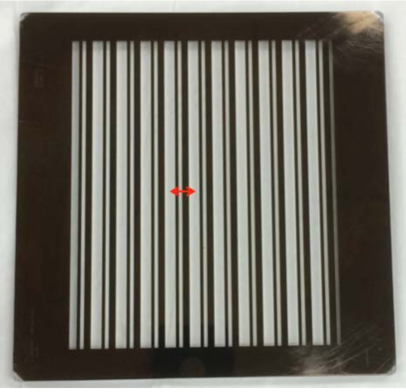

Fig. 5. Photograph of the 1D, rank-7 MURA shadow mask. The double arrow indicates the base period of the MURA.

As described in the previous simulation papers [5,6], selection of the coded-aperture pattern is a balance between the overall size of the base pattern and the resolution of the readout device. In short, the mask contains many cycles of the base pattern since one must observe the shadow from a complete pattern in order to obtain good image reconstruction. The light spots from events at the bottom of the crystal (closest to the mask and MAP readout) will have the smallest width at the mask plane, with the size determined by the thickness of light pipe between the bottom of the crystal and the mask. Balancing this criterion (which pushes one toward a smaller base mask pattern size) is the fact that repetition of the base pattern means one must be able to localize an event to a single pattern without using the coded-aperture approach, because the coded-aperture reconstruction can only localize the event within a pattern. If the event is ascribed to the wrong cycle of the pattern, then it will be incorrectly located in the mask imaging direction by the same integer number of patterns that the event was misplaced in the initial localization (see Section 3 on data analysis). This condition is important for events at the top of the crystal (those that fall the furthest from the mask and MAPs), since these are the ones that will be most diffuse and thus hardest to locate. This tends to drive the design toward a larger base mask pattern size. At the same time, the size of the smallest mask feature projected onto the MAP photocathodes must be large enough to be resolved by the MAP. This impacts the number of pixels within a given pattern (rank) and the length of the light pipe between the mask and the MAPs. The larger the distance, the more the magnification of the pattern, making it easier to resolve the mask feature size, but also the wider the pattern will be, making it harder to localize the event to the correct mask pattern.

The Hamamatsu 9500 MAPs used here have a primary pixel pitch of 3.04 mm. Based on a crystal emulation thickness of 20 mm, and balancing the terms described above, we used a minimum magnification of 2.14 for an event at the top of the crystal. With a base pattern size at the mask for a 24.85-mm-thick light pipe below the emulated crystal, this implied the use of the rank-7 pattern with a pitch of 1.4 mm. These values correspond to magnification factors of 2.23 to 4.82, giving base MURA feature sizes at the MAP varying from 3.12 to 6.75 mm or 1.02 to 2.2 pixels, respectively.

3 DATA COLLECTION

Data were collected with the rank-7 photomask described in Section 2.3 above. The overall geometries studied are summarized in Table 1. At least 20,000 events were collected at each depth with the acquisition system triggered by the last dynode signal of the center H9500.

The conceptual design of the hardware was meant to allow the amount of light pipe between the mask and the crystal to be changed without changing the alignment between the collimator, the mask, and the MAPs. However, this was not found to work well in practice. In fact, the whole assembly was sometimes rebuilt between measurements with different light pipe thicknesses. Consequently, the transverse location of the beam varied somewhat between the different measurements. As discussed below, an additional complication was that at times the order of the MAPs was changed, which affected the gains (and quantum efficiency) for the different strips.

Table 1
Emulated event depths and results.

Mask to crystal center (mm)	Emulated event depth in crystal (mm)	Depth resolution FWHM (mm)	In-crystal depth resolution FWHM (mm)	In-crystal depth resolution, crystal thickness deconvolved FWHM (mm)	X-resolution FWHM (mm)	X resolution source-width deconvolved FWHM (mm)
6.5	0.0	0.65	1.03	<0.54	1.67	1.43
9.0	4.0	0.65	1.03	<0.54	1.22	0.87
13.0	10.3	0.65	1.03	<0.54	1.45	1.17
20.7	22.5	1.67	2.65	2.50	1.16	0.78

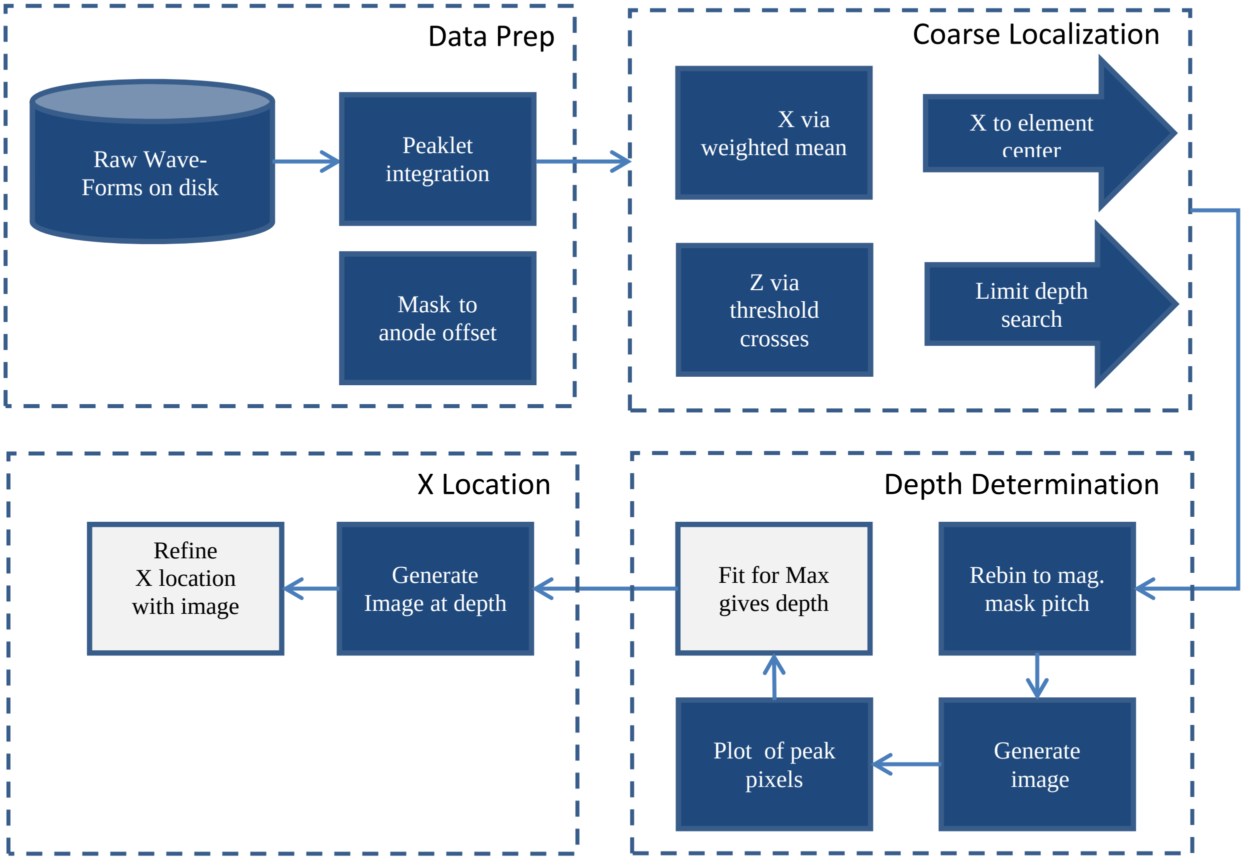

Fig. 6. Schematic diagram of the event processing steps.

3.1 DATA ANALYSIS

A number of different data processing approaches were explored to optimize the results obtained with the system. The final approach used is shown schematically in Fig. 6 and is described in detail below.

3.1.2 Preprocessing

Before individual events could be processed, we had to determine the alignment between the mask pattern and the MAP anodes for each measurement because of alignment shifts when the system was reconfigured. Knowledge of this alignment impacts rebinning the events for depth processing because the MAP anode spacing is not uniform but varies at the edge of the tube and has a gap between tubes. To determine the alignment, all of the events for a given depth were reconstructed using the coded-aperture cross-correlation technique and *the known* event depth and mask cycle. The average of the x-location obtained was then used as the known offset between the two patterns (mask and anode) for processing individual events for each emulated depth.

Ideally, the data would also have been corrected for spatial variations in the MAP gain and quantum efficiency. Unfortunately, these were not characterized and, worse, the MAP positions were exchanged for some of the configurations. To correct for the most egregious variations that occurred at tube boundaries, an assumption was made that the total light from many events should yield a smooth distribution. When the response for the unprocessed events was plotted as a function of anode strip number, discontinuities at the interface between tubes were sometimes noted and here gain variations were applied to provide a smoothed response.

Once the overall gains were set, the individual event data were processed using the peaklet integration technique discussed in Section 2.2. An energy threshold was used to keep only events in the main peak at 356 keV from the ^{133}Ba source used for the measurements. Because of the finite MAP area, the thick light pipe geometries, and the blackened sides of the system, the total light collected varied by 8.5% between events emulated at the top and bottom of the 2-cm-thick crystal. The energy cut was selected separately for each depth to avoid contamination with the

81-keV line from the source and by lead and tungsten K-Shell x-rays for events with the thinner light pipes that would have occurred with a single wide threshold used for all depths. (Analytical calculations [14] and simulations show this is a much smaller effect if a larger readout area is used.)

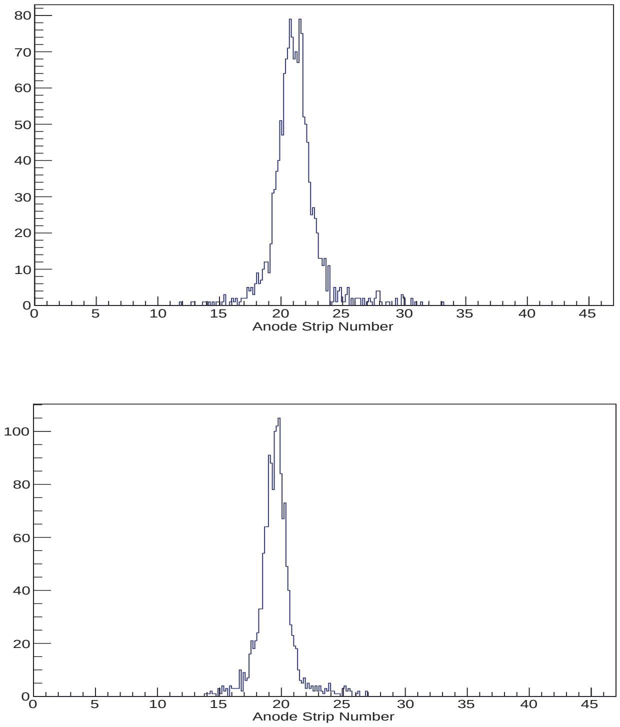

Fig. 7. Histograms of event x-locations at the bottom (bottom) and top (top) of the emulated crystal found using a weighted mean.

3.1.2 Coarse Event Localization

The first step in processing the individual events was to determine the coarse event location in x (along the direction of mask modulation) in order to localize the event to a single cycle of the mask pattern. A simple weighted mean was found to give the best results, and sample histograms of event distributions are shown in Fig. 7.

With a known coarse x-location, a rough estimate of the depth was obtained by counting the number of times that the ADC counts per channel vs channel numberfor an event exceeded a threshold set at 40% of the maximum value for the event. This worked because the broader the light spot at the mask, the more open and closed elements are shadowed and hence the more crossovers occur. The overall distributions of crossovers for events at the top and bottom of the emulated crystal are shown in Fig. 8. The strong peaks at even numbers are due to the fact that if the signal goes over the threshold, it generally also comes back down. The information was used to limit the lowest depths over which the finer depth determination was performed, both to increase processing speed and to reduce crosstalk that was found to occur between events at the top and bottom emulated locations.

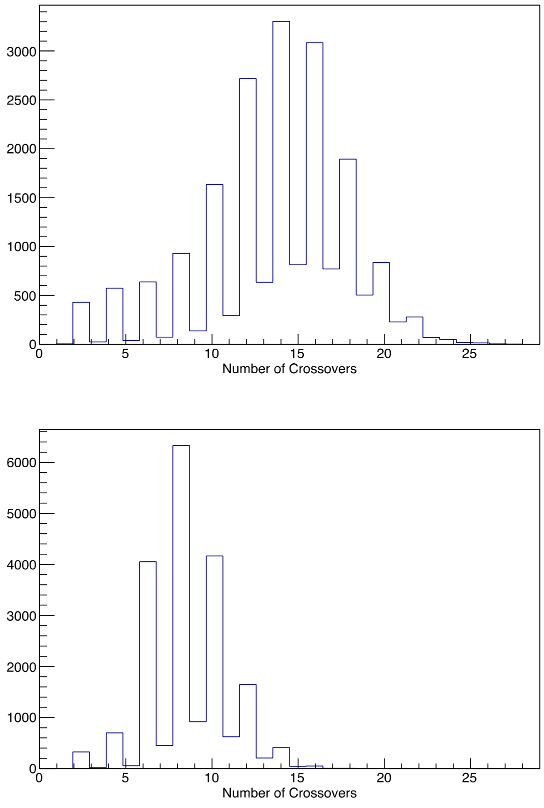

Fig. 8. Histograms for the number of crossovers (see text) for all events launched from the top (top) and bottom (bottom) of the emulated crystal.

3.1.3 Depth Determination

After the coarse x and depth locations had been determined, the center of the mask element nearest the x-location was chosen as the “starting” event x-location, and precise depth determination was performed. For this, the data were processed for a range of depths by generating a 1D coded-aperture image using the correct magnification and binning for that depth. This amounts to “refocusing” the system *a posteriori* to obtain the sharpest image. Sample images for a single event at a number of reconstructed depths are given in Fig. 9. As can be seen, as one varies the reconstruction depth, a degraded image progresses to a sharp point-source image, and then degrades again. A plot of the peak intensity versus reconstruction depth for the event is given in Fig. 10.

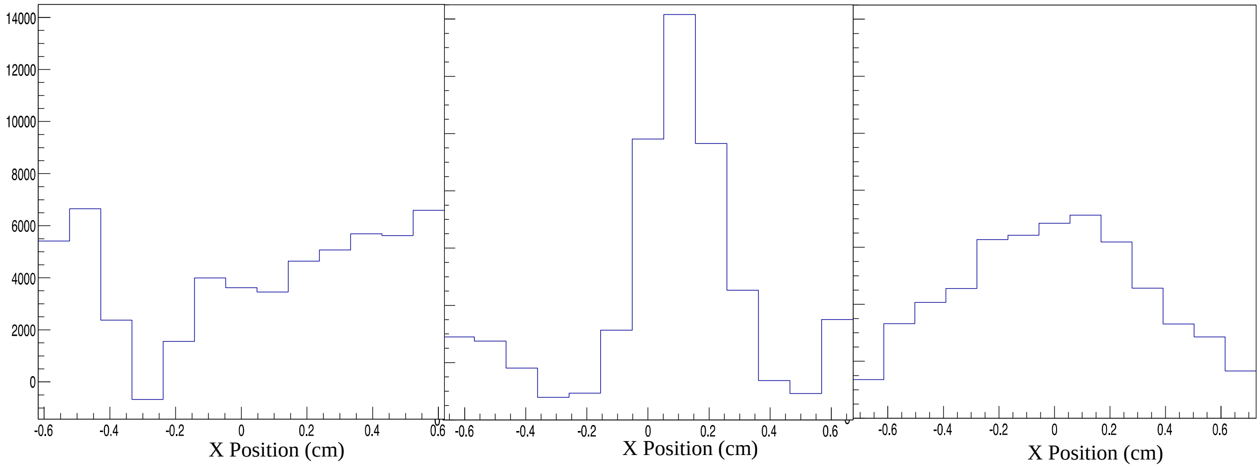

Fig. 9. From left to right, sample reconstructed images obtained using depths of 6.5, 9.2, and 12.0 mm, respectively. The peak is sharpest at the correct depth of 9.2 mm. A plot of peak height vs depth for this event is given in Fig. 10. The y-scale is arbitrary but the same for all plots.

To generate the image at each depth, the data were rebinned from the pitch of the anode strips to an idealized “detector” that had a pitch twice that of the magnified mask pattern for that depth, centered on the starting location. A standard cross-correlation reconstruction algorithm was then used [4] to generate the image. Note that the data from all strips were used, with the data from neighboring cycles of the mask folded back to the correct detector element representing the same part of the cycle [15]. To generate the rebinned detector values, the signal levels were weighted by the actual anode strip geometries, including the gaps between PMTs and the slightly greater width of the edge anodes of the PMTs

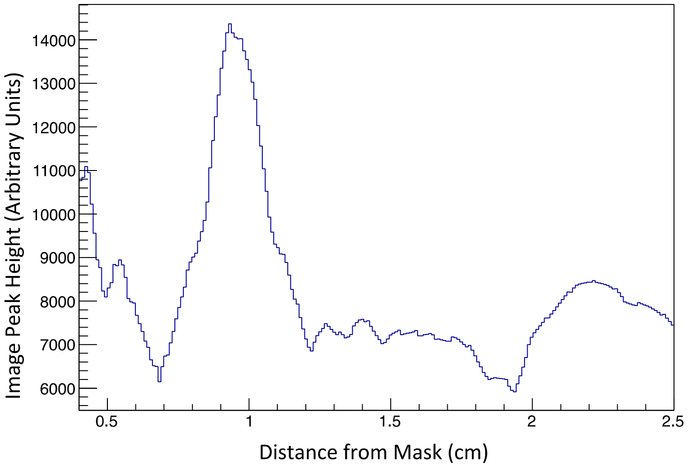

Fig. 10. Peak image value versus depth for a single event at an emulated location 9.2 mm from the bottom of the crystal. Sample single images for this event are shown in Fig. 9.

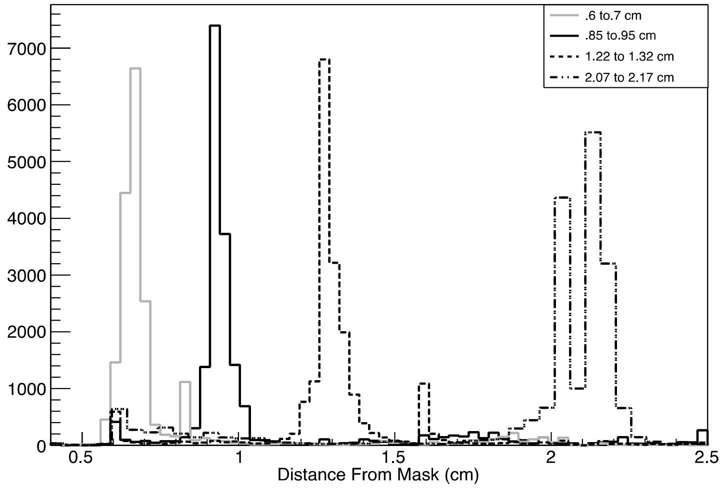

Fig. 11. Histograms of computed depths for the different emulated event depths.

The final depth results for the different emulated event depths are shown in Fig. 11. The FWHM of the peaks are given in Table 1. The results include the estimate of depth based on the system geometry (Depth Resolution FWHM), the results converted to locations inside a high index crystal (In-crystal depth resolution) and the technique’s capabilities in-crystal after deconvolution of the thin crystal thickness (In-crystal depth resolution, crystal thickness deconvolved).

Note that for the events at the top of the crystal, the bimodal structure observed in the data is also seen in light transport simulations, indicating that the structure is not just a statistical artifact.

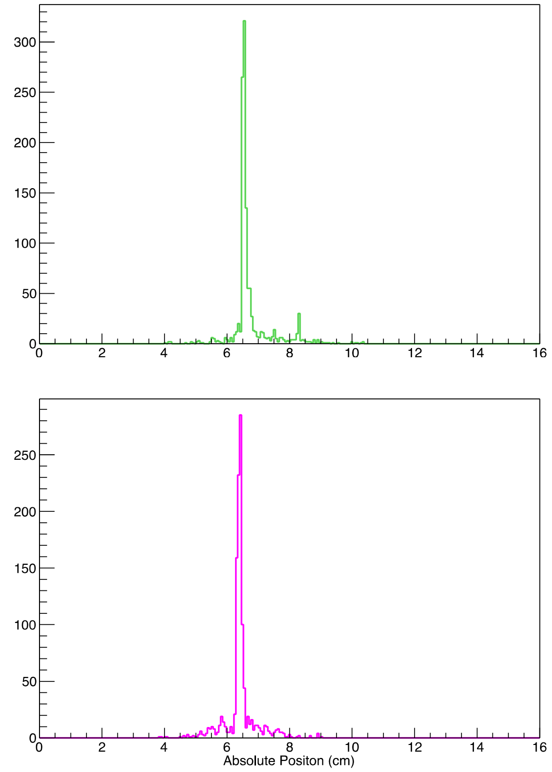

Fig. 12. Final x-distributions for event depths at the bottom (bottom) and top (top) of the crystal.

3.1.4 X-Location

The final step in the event localization was to use the reconstructed image from the determined depth to correct the starting x-location to its final value. The weighted mean of the peak location was determined from the image of the event to get a position finer than the pixel size of the coded-aperture image at a given depth. Histograms for the X-location for all of the events at each depth are given in Fig. 12.

5. DISCUSSION

The coded-aperture results clearly indicate that the technique works to obtain event locations in depth. In fact, initial results appeared to be too good to be true, with the FWHM of the different peaks of Fig. 11 being narrower than the 1-mm thickness of the crystal used in the experiment. Even after compensating for the 0.63 change in apparent thickness due to the difference in index of refraction between the light pipe and the crystal, the peak widths were just equal to the crystal thickness of 1 mm*. This led us to wonder if the crystal might be thinner than ordered and this was subsequently confirmed by a radiograph that gave a crystal thickness of 0.88 mm. A check with the crystal vendor indicated that the measured value was within their manufacturing tolerances. This indicates that the technique itself contributes little to the depth uncertainty for three of the four emulated depths, and consequently the deconvolved values in Table 1 for those depths are given only as an upper limit.

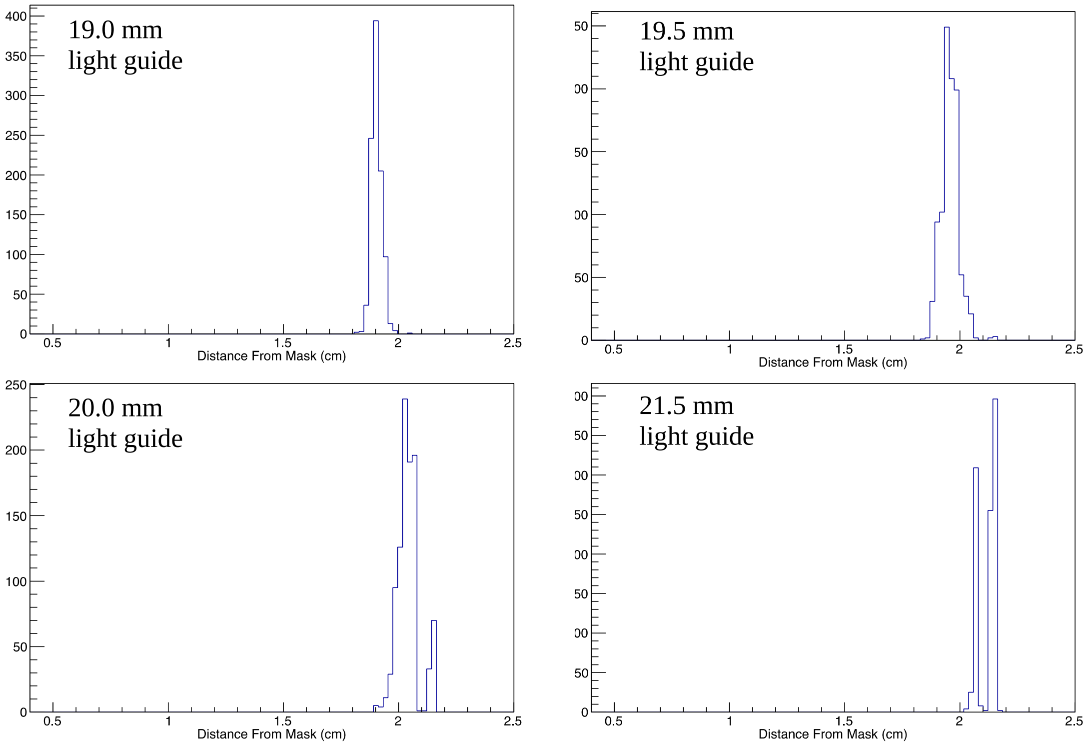

---

* Given the 356-keV of the gamma-ray events, events should occur almost uniformly throughout the depth of the thin crystal.

Fig. 13. Simulations showing development of a bimodal structure as emulated depth increases.

Unfortunately, the uncertainty in depth for the emulated location at the top of the crystal was significantly broader than 1 mm. Simulations indicate that this is a special case in that the simulated events show a bimodal distribution similar to that observed in the experimental data. In fact, simulations performed after the measurements were completed (Fig. 13) show that the response deteriorates just below the top location measured. This is likely due to a degeneracy of the depth finding algorithm and indicative of the fact that the rank-seven mask may only work over a finite range of depths. Better results might be obtained if a mask with more pixels was used. Simulations of a fully 2D readout using the current MAPs indicate that the bimodal peak structure is not an issue for a rank-19 system with a 3-cm-thick crystal. In addition, finer resolution readout devices are also available [16], but both the 2D system and one with a finer pitch require a significant increase in the number of readout channels. Experiments with them will have to wait until a more extensive data acquisition system can be assembled.

The performance in x-localization is equally compelling. The measured and unfolded widths of the different peaks are also given in Table 1. For some of the depths, the peak width is actually comparable to that of the beam at the crystal, indicating that we are not resolving the error due to the measurement technique. We note that the x-location was arbitrarily selected near the center of the crystal and that the x-scale of the measurements is determined from the theoretical resolution of the mask and is not determined by measuring events at different locations. While measurements at more x-locations would have been of value, the data acquisition system was only available for a limited time and additional measurements could not be made. We note that even if they had been made, the small size of the prototype would not have supported a wide range of locations. This is because for the thicker emulated geometries, the light spot at the

PMTs is large and the results would have included changes both due to the location above the coded aperture, and the location of the event with respect to the edge of the crystal. We wanted to avoid that complication. In the simulations reported earlier, a range of locations was sampled and the system behaved as expected [5,6]. A full probe of performance lateral to the crystal surface will require development of a system with a larger readout area.

6. SUMMARY

The results presented above indicate that the overall concept of using a shadow mask in the light pipe of a scintillator-based detector to improve position resolution is sound. The performance obtained with the 1D coded aperture agrees with simulations of the system, validating the full 2D simulations performed earlier and indicating that this approach could, for the first time, allow fine resolution of event locations in bulk scintillators.

7. ACKNOWLEDGEMENTS

This work was supported by the U.S. Department of Energy National Nuclear Security Administration Office of Defense Nuclear Nonproliferation Research and Development. The manuscript has been authored by the Oak Ridge National Laboratory, managed by UT-Battelle LLC under Contract No. DE-AC05-00OR22725 with the US Department of Energy. The US Government retains and the publisher, by accepting the article for publication, acknowledges that the US Government retains a nonexclusive, paid-up, irrevocable, worldwide license to publish or reproduce the published form of this manuscript, or allow others to do so, for US Government purposes.

8. REFERENCES

1. H.O. Anger, Reviews of Scientific Instruments 29 (1958) 27.
2. M. Ricard, Reviews of Scientific Instruments 527 (2004) 124.

3. J. Kataoka, et al., Nuclear Instruments and Methods in Physics Research Section A 732 (2013) 403.

4. E.E. Fenimore, T.M. Canon, Applied Optics 17 (1978) 337.

5. K.P. Ziock, et al, Proceedings of SPIE 8542 (2012) 854210-1-854210-12.

6. K.P. Ziock, M.A. Blackston, T. Van Vuure, IEEE Transactions on Nuclear Science, 60 (2013) 1390.

7. Hamamatsu Photonics, www.hamamatsu.com/us/en/product/category/3100/3002/H9500/index.html.

8. S.R. Gottesman, E.E. Fenimore, Applied Optics 28, (1989) 4344.

9. BC-630 from Saint-Gobain Crystals, 17900 Great Lakes Parkway, Hiram, OH 44234.

10. S. Agostinelli, et al., Nuclear Instruments and Methods in Physics Research Section A 506 (2003) 250.

11. Strück model SIS3316-250-14, http://www.struck.de/sis3316.html.

12. Phillips Scientific, http://www.phillipsscientific.com/pdf/776ds.pdf.

13. Toppan Photomasks, 131 E. Old Settlers Blvd, Round Rock, TX 78664.

14. J. Braverman, M. Harrison, K.P. Ziock, Proceedings IEEE Nuclear Science Symposium, Anaheim, CA, Oct. 29–Nov. 3, 335–338 (2012).

15. K.P. Ziock et al., Nuclear Instruments and Methods in Physics Research Section B 505 (2003) 420.

16. Photonis Planacon detector, http://www.photonis.com/en/ism/63-planacon.html.